Supporting Information

XRDMatch: A Semi-Supervised Learning Framework to Efficiently Discover Room Temperature Lithium Superionic Conductors

Table of contents:

1. Methods

1.1 Pseudo-label and consistency regularization

Pseudo-label is one of the earliest types of SSL algorithms [1], represented by the self-training algorithm [2,3]. Its workflow is based on an existing model, which makes predictions on unlabeled data and adds the predicted results as pseudo labels to turn them into “labeled data” to supplement the model. However, the biggest challenge of pseudo-label is how to ensure the correctness and coverage of the pseudo-labels. As the model predictions are not entirely correct, some wrongly labeled data may be added to train the network, which then affects the overall performance of SSL, known as the confirmation bias problem [1]. To improve the accuracy of the selected pseudo labels, confidence thresholding [4] was proposed where a probability threshold will be set to select only reliable pseudo labels. Another common approach in SSL is consistency regularization [5–7], which leverages unlabeled data to improve the performance. The method is based on the assumption that if two similar data points are close in high-dimensional space, their corresponding outputs should also be close. The same data is split into two branches, and different perturbations with different strengths are added to each branch. The model should perform better on the weaker perturbation branch, and its prediction is then used to generate pseudo labels. The stronger perturbation branch increases the diversity of the unlabeled dataset, which helps to enlarge the margin of the decision boundary. The pseudo labels and the strongly-augmented images are then used to minimize the cross-entropy loss to encourage the model’s prediction to be close to the true label distribution.

1.2 Implementation details of data augmentation for XRD data

As stated in the article, the XRDMatch algorithm employs two versions of data augmentation, referred to as "weak augmentation" and "strong augmentation". Common data augmentation techniques used in the computer vision field, such as flipping, rotation, cropping, scaling, and color jittering, are not suitable for one-dimensional XRD data. XRD provides a wealth of structural information, including

lattice constants, crystal structure, bond lengths, and bond angles, all of which are critical for determining the properties of materials. Material properties are intricately linked to the specific selection and arrangement of molecules within the material, resulting in each material having unique characteristics. From a data-centric perspective, the XRD shape factor itself is a one-dimensional signal comprising hundreds to thousands of points. Each of these points represents a potential feature or degree of freedom that can be harnessed to distinguish different materials. Similar materials tend to behave as similar features. Recently, Oviedo et al. [8] proposed a physics-based data augmentation method that successfully identified target material groups using peak scaling, peak elimination, and peak shifting for training the machine learning model. This approach resembles the way professional materials scientists analyze XRD data. Traditional methods for identifying compounds of interest and constructing phase diagrams for composite materials often rely on matching the descriptors of their XRD patterns (e.g., peak position, intensity, and full width at half maximum or FWHM) with known databases [9]. In our work, the weakly augmented data only adopted the simplest peak shift strategy as data augmentation, perturbing XRD data within a certain range to generate diverse yet not overly distorted data. The strongly augmented data incorporated peak scaling, peak elimination, and peak shift strategies, employing more robust and complex data augmentation techniques to expand the model's boundaries and enhance its generalization performance. From a physical perspective, weak augmentation maintains the basic structure of the XRD pattern while introducing minor perturbations that mimic measurement noise or slight variations in experimental conditions. Strong augmentation, on the other hand, significantly alters the XRD pattern, simulating more drastic changes such as those that might occur due to substantial compositional or structural variations. XRD data can provide detailed physical information such as Bragg positions, peak intensities, and space groups, among other parameters. For material scientists, it is crucial to understand the method and implications of weak and strong augmentation of XRD data. Weak augmentation primarily affects the positions slightly, preserving the overall structural information while introducing variability. Strong augmentation can modify peak positions and intensities more significantly, potentially altering the inferred crystal structure or phase composition. The following specific details outline the steps involved in each augmentation strategy:

1. Peak Shifting:

Select the XRD spectrum to move left and right, and randomly move its position x() within a specified range (-δ, δ).

$$x(new) = x(old + random(-\delta, \delta)) \quad (1)$$

2. Peak Scaling:

Randomly select a percentage, W_s, of peaks within the XRD pattern to enhance. For each selected peak A at index i, add its amplitude to a factor randomly scaled within a specified range (1-ε, 1+ε).

$$A_i' = A_i \times random(1-\varepsilon, 1+\varepsilon) + A_i \quad (2)$$

3. Peak Elimination:

Peak Elimination: Randomly select a percentage, W_e, of peaks within the XRD pattern to be weakened or removed entirely. For each selected peak A at index i, either randomly multiply its amplitude by a specified range (0,1), or remove it.

$$A_i' = A_i \times random(0,1) \text{ or } A_i' = 0 \quad (3)$$

These detailed implementation steps, accompanied by the corresponding formulas, enable the generation of diverse and realistic XRD patterns for training machine learning models. The specified parameters δ, W_s, ϵ, W_e can be adjusted to control the magnitude of variations introduced during the augmentation process. For weakly-augmentation, δ set a to 150; For strongly-augmentation, set δ, W_s, ϵ and W_e to 300, 1, 0.12, and 0.12, respectively.

1.3 VGG-11 architecture

The core architecture of VGG-11 adheres to the style of VGGNet, featuring a sequence of interleaved convolutional and pooling layers designed to effectively capture the features of the input data. The network is divided into five sections, with the first four each section consisting of two convolutional layers and a pooling layer. Convolutional layers employ kernels of dimensions 16 x 1, 12 x 1, 8 x 1, and 4 x 1, with kernel sizes progressively increasing to 64, 128, 256, 256, and 512. Through hierarchical stacking, the network's depth and complexity are gradually augmented. ReLU activation functions follow each convolutional layer to introduce non-linear characteristics. Subsequent to each convolutional layer is a pooling layer employing a 2 x 1 maximum pooling kernel with a stride of 2 to reduce the dimensions of the feature maps. At the tail end of the net structure, three fully connected layers, each comprising 1024 neurons, are employed. These layers are responsible for synthesizing the high-level features extracted by the convolutional and pooling layers, learning complex data representations through weighted connections. The ultimate output of the fully connected layers encompasses the network's classification predictions for the input images. Regarding hyperparameters, we opted for AdamW as the optimizer with a learning rate set at 0.0003, a batch size of 32, and a training duration of 100 epochs.

1.4 Loss function

The loss function for the entire model is divided into two parts: supervised loss for the labeled dataset and unsupervised loss for the unlabeled dataset. The supervised loss is:

$$L_S = \frac{1}{B_L} \sum_{i=1}^{B_L} H\left(y_i, \mathrm{P}\left(y \middle| w\left(x_i^l\right)\right)\right) \quad (4)$$

where B_L is the batch size for labeled dataset, $H(\cdot)$ refers to cross-entropy loss, $w(\cdot)$

means the weakly data augmentation function, and P(y|x) is the output probability from the model. The unsupervised training objective for the unlabeled dataset is:

$$L_u = \frac{1}{B_U}\sum_{i=1}^{B_U} \lambda(\mathrm{P}_i) H\left(\hat{\mathrm{P}}_i, \mathrm{P}\left(y \middle| \Omega\left(x_i^u\right)\right)\right) \qquad (5)$$

B_U is the batch size of unlabeled dataset, which is usually set to μ times batch size of labeled dataset. We use $\Omega(\cdot)$ and $\hat{\mathrm{p}}_i$ to denote the strong data augmentation and the pseudo-labels from the weakly-augmented unlabeled data, respectively. Under optimal conditions, these pseudo-labels should aptly reflect the authentic labels of the unlabeled samples. However, using pseudo labels will bring some risks and challenges. The traditional FixMatch method uses a fixed threshold, which may not be suitable for all cases. The quality of samples with different labels in the dataset may vary, and the same threshold cannot balance the learning difficulty between samples of different categories. To address this issue, we drew inspiration from the course pseudo label strategy in the FlexMatch method [59] and incorporated the data filtering process into the training. By dynamically adjusting the threshold to retain high-quality pseudo label data, we combine it with the labeled data, creating a larger mixed dataset that incrementally improves model performance. We use λ(pi) to represent the dynamic confidence thresholding mechanism in XRDMatch：

$$\lambda(\mathrm{P}) = \mathrm{I}\left(\max(\mathrm{P}) > T_t\left(\arg\max(\mathrm{P})\right)\right) \qquad (6)$$

where T_t (arg max (p)) is the dynamic class-wise threshold, computed as:

$$\begin{aligned} \sigma_t(c) &= \sum_{n=1}^{N} \mathrm{I}\left(\max(\mathrm{P}) > \tau\right) \bullet \mathrm{I}\left(\arg\max(\mathrm{P} = c)\right), \\ \beta_t(c) &= \frac{\sigma_t(c)}{\max \sigma_t}, \\ T_t(c) &= \beta_t(c) \bullet \tau \end{aligned} \qquad (7)$$

where σ_t(c) refers to the learning effect of class c at time step t, β_t(c) is the normalization method, and β_t(c) is the flexible threshold of class c at time step t. with τ being the pre-defined global threshold and N is the total number of unlabeled data. The rationale behind the dynamic threshold formula is to ensure that the thresholds adjust gradually when the learning effect is modest and become more responsive as the learning effect becomes more pronounced. This adaptive thresholding mechanism assists in selectively identifying and incorporating higher-quality samples into the training process, ultimately enhancing the effective utilization of data during training. This approach ensures that the model is more discerning as it learns, focusing on samples that contribute more to its improvement as the training progresses.

1.5 Evaluation metric

F1 score is a machine learning evaluation metric that measures a model's accuracy. It combines the precision and recall scores of a model. The accuracy metric computes

how many times a model made a correct prediction across the entire dataset. The formula for calculating F1-score is as follows:

$$F1 = 2 \times \frac{precision \cdot recall}{precision + recall} \quad (8)$$

where precision and recall are defined as:

$$precision = \frac{TP}{TP + FP} \quad (9)$$

$$recall = \frac{TP}{TP + FN} \quad (10)$$

Precision is calculated by dividing the number of true positives (TP) by the sum of true positives (TP) and false positives (FP). Recall, also known as sensitivity or true positive rate, represents the proportion of true positive predictions among all actual positive samples. Recall is calculated by dividing the number of true positives by the sum of true positives and false negatives (FN).

1.6 Ab initio molecular dynamics (AIMD) simulations

The projected augmented wave (PAW) method combined with Perdew-Burke-Ernzerhof (PBE) functional [10] were employed to describe the interaction between ions and electrons. The initial structure was relaxed using a convergence criterion of 10^{-5} eV for energy and 0.01 eV/Å for atomic forces. A time step of 2 fs was used in the AIMD simulations. The initial structure was obtained through static relaxation, followed by an initial temperature of 100 K and subsequent heating to four different temperatures (1500 K, 1200 K, 900 K, and 600 K) over a period of 2 ps. AIMD simulations were performed using a Nosé-Hoover thermostat to control the temperature, followed by a 30 ps molecular dynamics simulation to investigate diffusion behavior. All calculations were performed on the Vienna Ab initio Simulation Package (VASP) software [11]. Employing AIMD simulations, we calculate the conductivity of the selected solid electrolyte candidates across a range of elevated temperatures (1500 K, 1200 K, 900 K, and 600 K). The Arrhenius equation enables us to derive the conductivity under these high-temperature conditions. Subsequently, we perform linear fitting methods on specific data points to obtain the conductivity at room temperature (300 K). The ionic diffusivity and conductivity were calculated using a module from the pymatgen library [12], which offers analysis tools for examining diffusion in materials.

1.7 Van Hove correlation functions

The van Hove correlation function is divided into two components: the self-part $G_s(r,t)$ and the distinct-part $G_d(r,t)$, expressed as:

$$G_S(r,t)=\frac{1}{4\pi r^2 N_d}\left\langle \sum_{i=1}^{N_d}\delta\left(r-\left|r_i(t_0)-r_i(t+t_0)\right|\right)\right\rangle_{t_0} \quad (11)$$

$$G_d(r,t)=\frac{1}{4\pi r^2 \rho N_d}\left\langle \sum_{i\neq j}^{N_d}\delta\left(r-\left|r_i(t_0)-r_j(t+t_0)\right|\right)\right\rangle_{t_0} \quad (12)$$

In these expressions, N_d is the number of reference ions in the system, r is the radial distance being measured from reference ion, ρ is the average number density of ions, δ() represents the Dirac delta function, and the angle brackets indicate averaging over all initial times t_0. The position of the i-th particle at time t is denoted as $r_i(t)$, and the position of the j-th other particle at time t is denoted as $r_j(t)$. The self-part $G_s(r,t)$ reflects the likelihood that a particle has moved a distance r from its starting point after a time t, while the distinct-part $G_d(r,t)$ provides the spatial distribution of other particles relative to a reference particle after time t. To ensure that $G_d(r,t)$ approaches unity as $r \rightarrow \infty$, the average particle density ρ is used as a normalization factor. Notably, at $t = 0$, the distinct-part $G_d(r,t)$ reduces to the static pair correlation function, g(r), which is widely utilized to study the structural arrangement of particles at equilibrium.

2. Results and Discussion

2.1 Implementation details of ensemble learning

Ensemble learning, a technique also known as committee-based learning, offers a means to enhance prediction accuracy by combining the predictions of multiple models. Through voting or weighting methods, the predictions from various models are amalgamated, mitigating individual model biases or noise and thus improving prediction accuracy and robustness. To enhance model diversity, we adopt the Random Sampling method, wherein each model is trained on a dataset comprising 10 randomly selected SIC labels, 10 randomly selected Non-SIC labels, and 80% unlabeled labels. As illustrated in Figure S8, during the prediction process, a direct voting approach is implemented, with each model providing a prediction and adherence to the majority decision principle.

2.2 Table S1 ~ S2

Table S1. Classification reports for individual and ensemble models. three indicators (precision, recall, F1 score) were used to evaluate the performance of the model.

Model	1	2	3	4	5	6	7	8	9	10	Ensmble
Precision	0.83	0.78	0.76	0.73	0.86	0.80	0.74	0.79	0.73	0.74	0.92
Recall	0.76	0.77	0.75	0.80	0.70	0.74	0.74	0.71	0.73	0.71	0.92
F1 score	0.79	0.77	0.76	0.75	0.75	0.74	0.74	0.74	0.73	0.73	0.92

Table S2. SICs from unlabel database predicted by XRDMatch models. Total 200 structures were predicted to be SICs structures.

ICSD_ID	Formula	Output frequency	Label	Similarity	ref
icsd_1258	$GeLi_{1.08}Zn_{0.92}$	6	X	0.5	-
icsd_1984	Li_2MnCl_4	6	1	0.66	13
icsd_10398	$K_6LiFe_{24}S_{26}Cl$	6	X	0.92	-
icsd_16185	$SrLiTa_2O_6F$	7	X	0.66	-
icsd_16789	LiMgN	5	1	0.98	14
icsd_25515	Li_3OI	7	0	0.94	15
icsd_25586	$Li_{7.2}Ti_{0.8}N_{2.4}O_{1.6}$	5	X	1	-
icsd_26540	$Li_{2.94}N$	7	0	1	16
icsd_28697	$LiBiS_2$	9	X	0.9	-
icsd_29115	$Li_4NaKAl_4Be_3B_{10}O_{27}$	6	X	0.59	-
icsd_33865	Li_2MnBr_4	6	1	0.61	13
icsd_37370	$LiND_2$	9	1	0.45	17
icsd_38414	$Ga_{1.96}Li_{0.12}S$	7	X	0.54	-
icsd_40194	Li_2MnBr_4	5	1	0.99	13
icsd_40456	$LiSbS_2$	9	0	0.94	18
icsd_40664	Li_2MnBr_4	5	1	0.53	13
icsd_41403	$LiInSe_2$	9	X	0.89	-
icsd_41466	$Li_{0.45}Y_{0.45}Zr_{0.55}S_2$	5	X	0.66	-
icsd_41468	$Li_{0.95}Y_{0.95}Zr_{0.05}S_2$	6	X	0.99	-
icsd_43938	$CuLi_2As$	6	X	0.95	-
icsd_44815	$LiNdS_2$	7	X	0.97	-
icsd_44824	LiZnP	6	X	0.97	-
icsd_44827	$LiSmS_2$	7	X	0.97	-
icsd_44828	$LiGdS_2$	9	X	0.98	-
icsd_44830	$LiYS_2$	5	0	0.99	19
icsd_44831	$LiDyS_2$	6	X	0.98	-
icsd_44832	$LiHoS_2$	6	X	0.98	-
icsd_44833	$LiErS_2$	5	X	0.98	-
icsd_44834	$LiSmSe_2$	6	X	0.96	-

icsd_44835	$LiGdSe_2$	7	X	0.97	-
icsd_44837	$LiYSe_2$	8	X	0.98	-
icsd_44838	$LiDySe_2$	6	X	0.98	-
icsd_44839	$LiHoSe_2$	5	X	0.98	-
icsd_44840	$LiErSe_2$	8	0	0.98	20
icsd_44847	$LiPrS_2$	7	X	0.96	-
icsd_44939	$LiEuS_2$	6	X	0.96	-
icsd_49646	$Li_{7.2}N_{1.6}Cl_{2.4}$	5	0	0.99	21
icsd_50182	Li_3ErBr_6	6	0	1	22
icsd_50305	$Li_{1.9}Mn_{0.9}Ga_{0.1}Cl_4$	5	0	0.67	23
icsd_50386	$Li_2U_{1.02}Br_6$	5	0	0.99	24
icsd_52814	$CdLi_2ZnP_2$	6	X	0.97	-
icsd_53094	$LiInSe_2$	6	X	0.89	-
icsd_53257	$CuFeLi_{0.9}S_2$	5	X	0.98	-
icsd_53299	$Cu_{0.39}Li_{2.6}N$	6	0	0.94	25
icsd_53433	$EuLiS_2$	9	X	0.96	-
icsd_53493	$Fe_3LiSn_2S_8$	7	X	0.65	-
icsd_56481	$LiTiCl_3$	5	X	0.66	-
icsd_61337	$LiGaBr_4$	6	X	0.56	-
icsd_62248	$LiTiCl_3$	5	X	1	-
icsd_67259	Li_2CrCl_4	7	1	0.67	26
icsd_68380	Li_2FeS_2	5	X	0.99	-
icsd_69678	Li_2MnCl_4	6	1	0.66	13
icsd_69692	$LiCo_6P_4$	6	X	0.55	-
icsd_69877	Li_4OsD_6	5	X	0.62	-
icsd_72202	La_2LiSbO_6	5	1	0.65	27
icsd_72211	$NaBaLiNiF_6$	6	X	1	-
icsd_72648	$Li_4ZnIn_2F_{12}$	7	X	0.64	-
icsd_73222	Li_2ZnCl_4	9	1	0.95	28
icsd_73223	Li_2ZnBr_4	9	1	0.96	28
icsd_73229	Li_2CoCl_4	6	1	0.67	29
icsd_73846	$SrPrLiTeO_6$	8	X	0.66	-
icsd_73951	Li_2FeCl_4	7	1	0.67	30
icsd_73952	Li_2FeCl_4	6	1	0.67	30
icsd_74313	$SrLi_{0.25}Ru_{0.75}O_4$	5	X	1	-
icsd_74871	$Li_{1.6}Mn_{1.2}Cl_4$	7	1	0.66	31
icsd_74957	Li_2MgCl_4	6	1	0.65	13
icsd_74959	Li_2VCl_4	7	1	0.85	13
icsd_80511	$LiMg_2RuD_7$	6	X	0.86	-
icsd_82199	Li_2FeBr_4	7	1	0.62	31
icsd_82201	Li2FeBr4	8	1	0.66	31
icsd_84978	$In_{16}Fe_8Li_{0.7}S_{32}$	6	X	0.66	-
icsd_84979	$In_{16}Fe_8Li_{5.2}S_{32}$	5	X	0.66	-

icsd_84980	$In_{16}Fe_8Li_{12.2}S_{32}$	7	X	0.66	-
icsd_84981	$In_{16}Fe_8Li_{16.4}S_{32}$	6	X	0.66	-
icsd_86012	$Li_{1.2}Lu_{0.4}U_{0.4}S_2$	7	X	0.99	-
icsd_86013	$Li_{1.08}Lu_{0.46}U_{0.46}S_2$	6	X	0.99	-
icsd_91810	$La_{0.5}Li_{0.5}TiO_3$	7	0	0.62	32
icsd_92238	$La_{0.5}Li_{0.5}TiO_3$	5	0	0.88	32
icsd_92306	$Li_4Na_2N_2$	5	0	1	18
icsd_93258	$Li_{0.51}Mg_{2.49}N_{1.83}$	5	X	0.89	-
icsd_93260	$Li_{1.12}Mg_{0.88}N_{0.96}$	6	X	0.97	-
icsd_95639	$Li_{1.9}Fe_{1.05}Cl_4$	5	1	0.66	33
icsd_95787	$RbLiND_2$	5	X	0.91	-
icsd_95939	$Li_{2.92}N$	8	0	1	16
icsd_96915	$LiGaSe_2$	7	X	0.51	-
icsd_97487	La_2LiRuO_6	5	X	0.66	-
icsd_98263	$La_{0.522}Li_{0.432}TiO_3$	8	0	0.62	32
icsd_98265	$La_{0.531}Li_{0.396}TiO_3$	7	0	0.62	32
icsd_98647	$Li_{2.93}Ni_{0.07}N$	6	0	0.91	34
icsd_98649	$Li_{2.94}Cu_{0.06}N$	7	0	0.93	25
icsd_98979	$La_{0.606}Li_{0.183}TiO_3$	5	0	0.53	32
icsd_102519	$Co_{0.46}Li_{2.54}N$	5	0	0.92	35
icsd_104788	$Li_{23}Sr_6$	6	X	0.96	-
icsd_106630	$Eu_{0.5}Li_{0.5}S$	9	X	0.96	-
icsd_106708	$GaIrLi_2$	5	X	0.99	-
icsd_106945	$Cu_4In_{20}Li_4S_{32}$	7	X	0.65	-
icsd_106946	$Cu_4In_{20}Li_6S_{32}$	8	X	0.65	-
icsd_106948	$Li_4In_{16}Sn_4S_{32}$	7	X	0.58	-
icsd_106949	$Li_8In_{16}Sn_4S_{32}$	7	X	0.58	-
icsd_108886	Li_2O	8	X	0.56	-
icsd_150411	$SrLi_{0.3}Nb_{0.5}W_{0.2}O_3$	6	X	0.66	-
icsd_150451	$Li_{0.2}Na_{0.27}La_{0.5}TiO_3$	6	1	0.62	36
icsd_150452	$Li_{0.2}Na_{0.3}La_{0.5}TiO_3$	7	1	0.62	36
icsd_150453	$Li_{0.2}Na_{0.312}La_{0.477}TiO_3$	7	1	0.62	36
icsd_150455	$Li_{0.2}Na_{0.186}La_{0.525}TiO_3$	7	1	0.62	36
icsd_152890	K_2LiAlH_6	5	X	0.98	-
icsd_154316	$Li_{1.8}Na_{0.2}MgCl_4$	8	1	0.65	13
icsd_155633	$La_{0.55}Li_{0.35}TiO_3$	5	0	0.62	32
icsd_156000	$LiND_2$	10	1	0.45	17
icsd_157628	$Li_6SrLa_2(NbO_6)_2$	7	0	1	37
icsd_161361	$La_{0.67}Li_{0.33}MnO_3$	7	X	0.62	-
icsd_161387	$Li_6La_2Sr(NbO_6)_2$	7	0	1	37
icsd_163860	$Li_6CaLa_2Ta_2O_{12}$	5	1	1	38
icsd_164890	$K_3Li_2(NbO_3)_5$	5	X	0.6	-
icsd_164921	$Li_{0.5}Ga_{0.5}Cr_2S_4$	8	X	0.66	-

icsd_164922	$Li_{0.5}In_{0.5}Cr_2S_4$	8	X	0.65	-
icsd_165469	$Li_{0.5}La_{0.5}TiO_3$	7	0	0.88	32
icsd_165480	$Li_{0.5}La_{0.5}TiO_3$	5	0	0.88	32
icsd_165481	$Li_{0.3}Na_{0.2}La_{0.5}TiO_3$	7	0	0.88	36
icsd_165487	$Li_{0.2}Na_{0.3}La_{0.5}TiO_3$	6	1	0.88	36
icsd_166510	Li_2LiVCl_4	7	1	0.67	13
icsd_166525	$RbLi_{0.5}Cr_{1.5}F_6$	5	X	0.66	-
icsd_167577	$Li_{0.48}Mg_{2.52}N_{1.84}$	7	X	0.89	-
icsd_167581	$Li_{1.11}Mg_{0.89}N_{0.96}$	6	X	0.97	-
icsd_167582	$Li_{1.04}Mg_{0.96}N_{0.98}$	6	X	0.97	-
icsd_167584	$Li_{1.10}Mg_{0.90}N_{0.96}$	6	X	0.97	-
icsd_167585	$Li_{1.09}Mg_{0.91}N_{0.97}$	5	X	0.95	-
icsd_170261	$LiEu_2NCNI_3$	5	X	0.66	-
icsd_172040	$Pr_2BaLiRuO_7$	5	X	0.55	-
icsd_172041	$La_2BaLiRuO_7$	5	X	0.55	-
icsd_172044	$Li_{0.3}La_{0.567}TiO_3$	5	0	1	32
icsd_180630	$Li_{0.3}Na_{0.2}La_{0.5}Nb_2O_6$	5	0	0.53	36
icsd_180631	$Li_{0.2}Na_{0.3}La_{0.5}Nb_2O_6$	7	1	0.53	36
icsd_180632	$Li_{0.1}Na_{0.4}La_{0.5}Nb_2O_6$	5	1	1	36
icsd_180633	$Li_{0.07}Na_{0.43}La_{0.5}Nb_2O_6$	6	1	0.53	36
icsd_180634	$Li_{0.04}Na_{0.46}La_{0.5}Nb_2O_6$	7	1	1	36
icsd_180635	$Li_{0.02}Na_{0.48}La_{0.5}Nb_2O_6$	7	1	0.53	36
icsd_181882	$Li_2O_{0.75}P_{0.25}$	8	X	1	-
icsd_181883	$Li_2O_{0.75}As_{0.2}$	9	X	0.96	-
icsd_182035	$Li_{2.25}H_{4.75}La_3Sn_2O_{12}$	6	1	1	39
icsd_182036	$Li_{4.59}H_{2.41}La_3Sn_2O_{12}$	6	1	1	39
icsd_182992	$LiZn_2(BD_4)_5$	6	X	0.66	-
icsd_183686	$Li_{6.5}La_3Ta_{0.55}Zr_{1.45}O_{12}$	6	0	1	40
icsd_187132	LiFeAs	5	X	0.5	-
icsd_188886	$Li_{10}GeP_2S_{12}$	7	0	1	41
icsd_189813	$Li_4Na_{12}Y_6Zr_6P_{12}C_4H_4O_{68}$	5	X	0.53	-
icsd_191542	$Li_{6.46}Al_{0.081}La_3Zr_2O_{12}$	7	0	1	42
icsd_193473	$Li_{3.72}H_{2.78}La_3Ta_{0.5}Zr_{1.5}O_{12}$	7	1	1	39
icsd_193755	$Li_{10}SnP_2S_{12}$	6	0	1	43
icsd_193768	Li_4SnSe_4	5	0	0.99	44
icsd_193947	$Li_{10.35}Ge_{1.3}P_{1.65}S_{12}$	9	0	1	45
icsd_195437	$Li_{4.92}La_3Ta_{1.56}Zr_{0.44}O_{12}$	5	1	1	46
custom_200008	$Li_{6.5}La_3Zr_{1.5}Ta_{0.5}O_{12}$	5	0	1	40
icsd_200046	$LiPdD_{0.70}$	5	X	0.99	-
icsd_201147	$Li_3Na(NH_2)_4$	7	1	0.45	47
icsd_202401	Li_6CoCl_8	5	1	1	48
icsd_202519	Li_2FeCl_4	8	1	0.53	30
icsd_202743	Li_2ZnCl_4	10	1	0.63	28

icsd_237141	$Li_6La_3Nb_{1.5}Y_{0.5}O_{12}$	5	0	1	49
icsd_237146	$Li_{6.5}La_3Nb_{1.25}Y_{0.75}O_{12}$	5	0	1	49
icsd_237808	$Li_{1.83}H_{4.21}La_3Sn_2O_{12}$	6	1	1	39
icsd_238335	$K_8Li_{2.29}Ge_{43.47}$	9	X	0.64	-
icsd_238336	$K_8Li_{2.29}Ge_{43.47}$	9	X	0.88	-
icsd_238338	$K_8Li_{2.45}Ge_{43.37}$	7	X	0.88	-
icsd_238340	$K_8Li_{2.48}Ge_{43.37}$	9	X	0.88	-
icsd_238688	$Al_{0.24}La_3Li_{6.28}Zr_2O_{12}$	5	0	1	42
icsd_238691	$La_3Li_{5.8}Zn_{0.6}Zr_2O_{12}$	5	1	1	50
icsd_238784	$Ba_6Nb_4TiLiO_{18}$	5	X	0.75	-
icsd_238986	$Li_{0.12}Na_{0.88}NbO_3$	6	X	0.75	-
icsd_245934	$Li_6SrLa_2Sb_2O_{12}$	5	X	1	-
icsd_245935	$Li_{6.4}Sr_{1.4}La_{1.6}Sb_2O_{12}$	6	X	1	-
icsd_247255	Li_8SeN_2	6	0	0.5	18
icsd_248115	$LiAsSe_2$	9	0	0.94	51
icsd_248116	$LiAsSe_2$	8	0	0.58	51
icsd_248118	$LiAsSe_2$	6	0	0.96	51
icsd_248307	$Li_{10}GeP_2S_{12}$	8	0	1	41
icsd_250804	$Li_{0.2}Ge_{0.6}Sb_{0.20}Te$	5	X	0.53	-
icsd_250860	$Li_5Ca_9B_7O_{21}F_2$	5	X	0.55	-
icsd_261833	$LiGdW_2O_8$	5	X	0.52	-
icsd_262644	$In_2Li_2SiSe_6$	5	X	0.62	-
icsd_291520	$Li_{0.16}Sr_{0.69}Ga_{0.25}Ta_{0.75}O_3$	5	1	0.86	52
custom_300101	Li_7PS_6	10	0	0.99	53
custom_300103	Li_6PS_5Cl	10	0	1	53
custom_300104	Li_6PS_5Br	7	0	0.99	53
icsd_380390	Li_6AsSe_4SeI	6	X	0.96	-
icsd_380451	$Ca_{5.45}Li_{3.55}Si_2F_{1.5}O_{12.45}$	7	X	0.66	-
custom_400004	$Li_{10}Ge(PS_6)_2$	7	0	0.52	41
icsd_411039	$La_{0.504}Li_{0.486}TiO_3$	7	0	0.62	32
icsd_412208	LiAuSn	6	X	0.94	-
icsd_415121	Li_2TeSe_3	5	X	0.56	-
icsd_417442	$Li_2Rh_3B_2$	6	X	0.48	-
icsd_417988	$Li_{1.1}Mg_{3.9}Rh_8B_4$	8	X	0.54	-
icsd_417989	$Li_8Mg_4Rh_{19}B_{12}$	5	X	0.48	-
icsd_418488	$Li_{6.192}PS_{5.24}Br_{0.757}$	8	0	0.99	53
icsd_418489	Li_6PS_5I	7	0	0.98	53
icsd_421130	$Li_7PS_4S_2$	10	0	0.99	53
icsd_421545	$Ba_6Li_2In_4N_{1.67}$	6	X	0.64	-
icsd_421959	$LiLa_{0.67}Ta_2O_6F$	5	X	0.66	-
icsd_421960	$Li_{1.25}La_{0.58}Nb_2O_6F$	6	X	0.66	-
icsd_423831	Li_2N_2	7	X	0.46	-

2.2 Figure S1 ~ S8

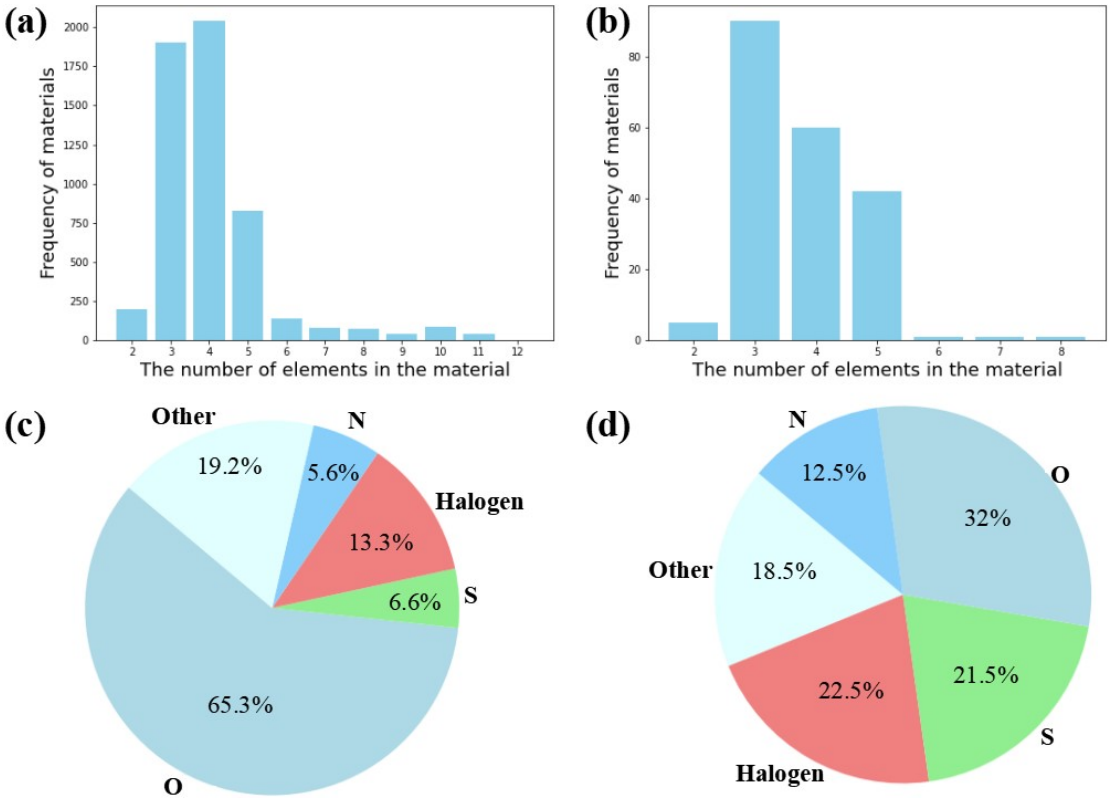

Figure S1. Comparison of statistical data between unlabeled and SICs from unlabel database predicted by XRDMatch models: (a)Frequency of elemental composition in compounds within the unlabeled database. (b)Frequency of elemental composition in compounds within the predicted materials. (c)Proportion of compounds based on elemental composition in the unlabeled database. (d)Proportion of compounds based on elemental composition in the predicted materials.

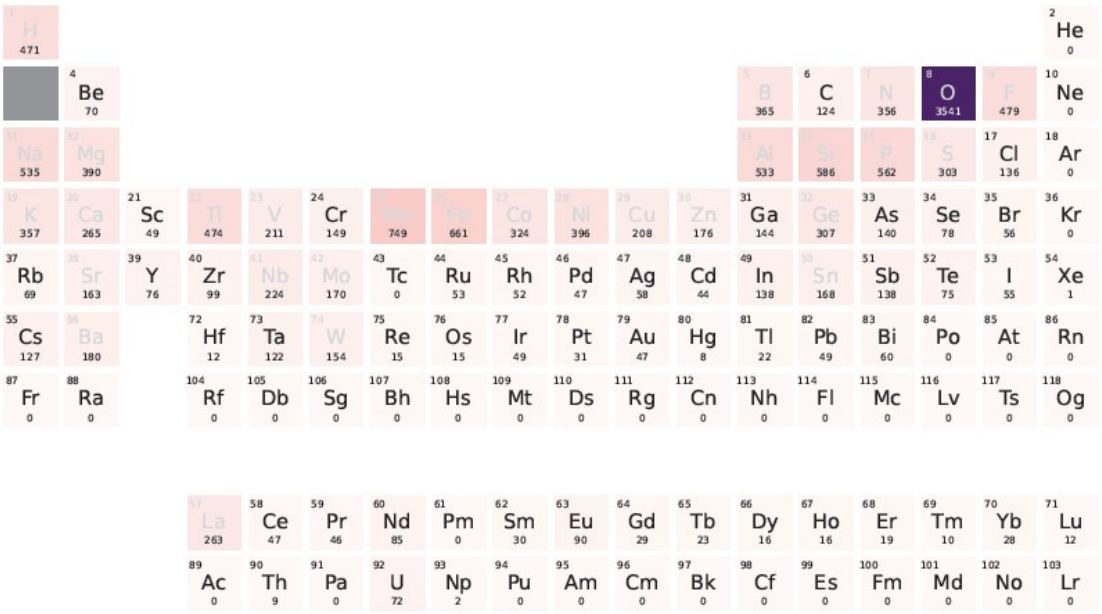

Figure S2. Number of each element from the periodic table in unlabel dataset.

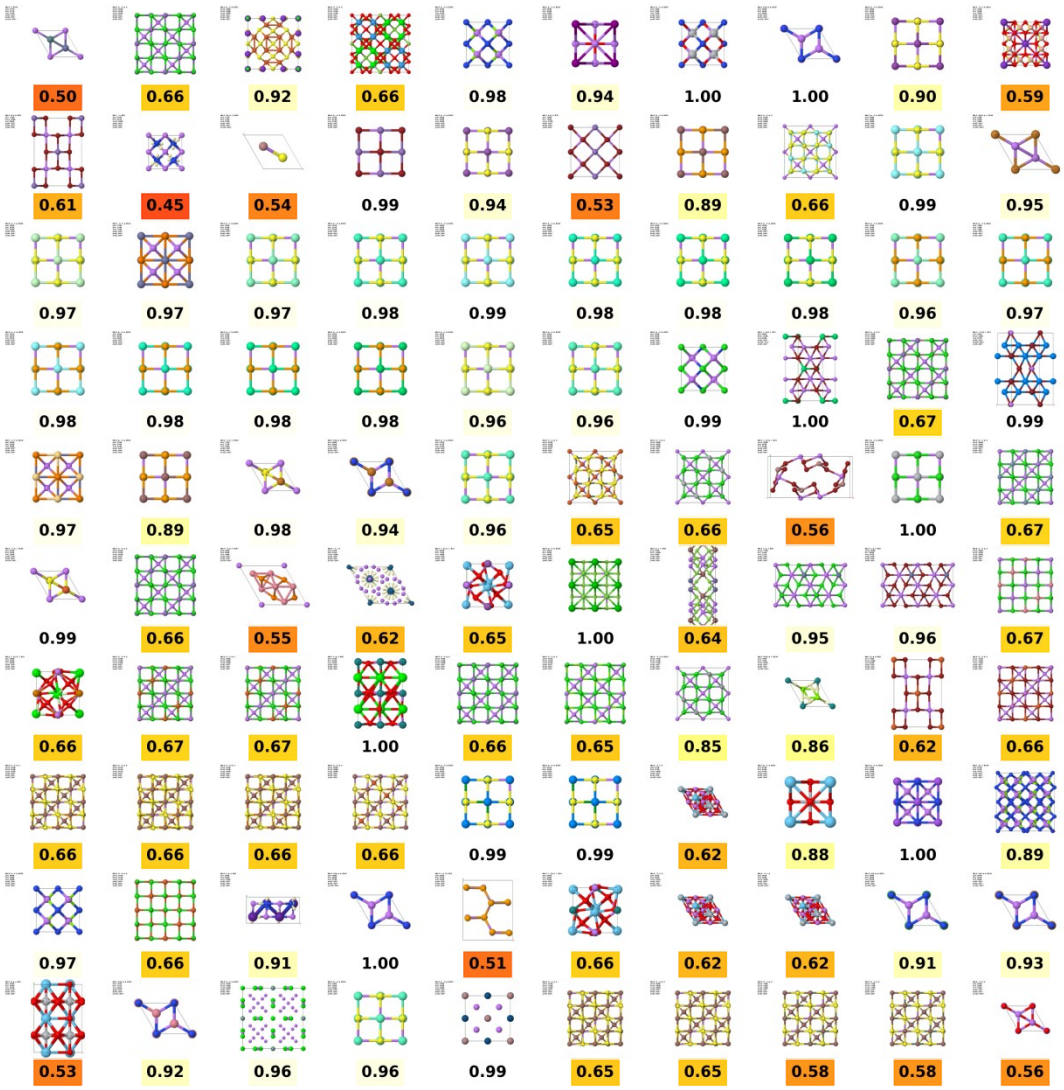

Figure S3. Visualization of the similarity between SICs from unlabel database predicted by XRDMatch models and SICs in the label database. (Top 100 data)

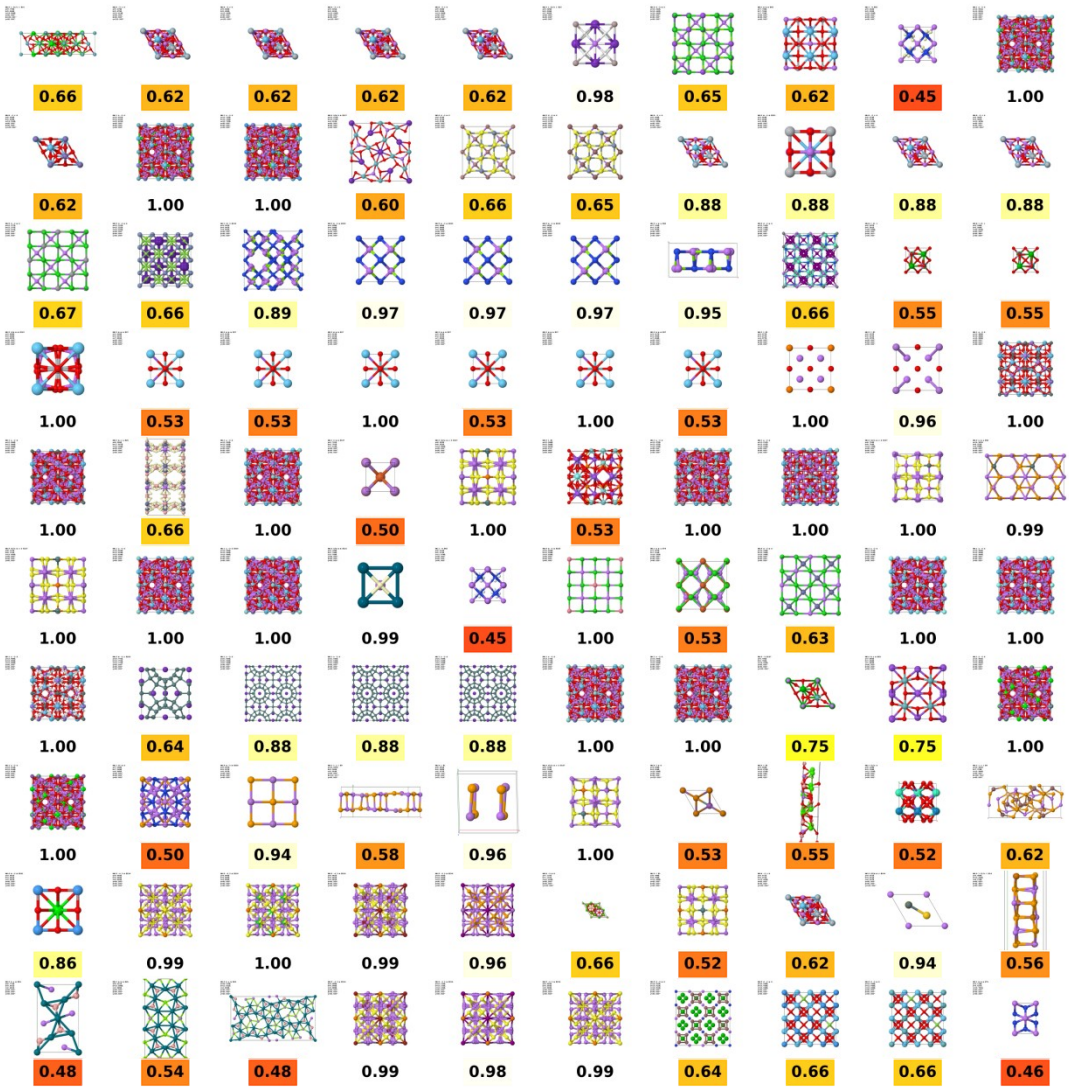

Figure S4. Visualization of the similarity between SICs from unlabel database predicted by XRDMatch models and SICs in the label database. (Last 100 data)

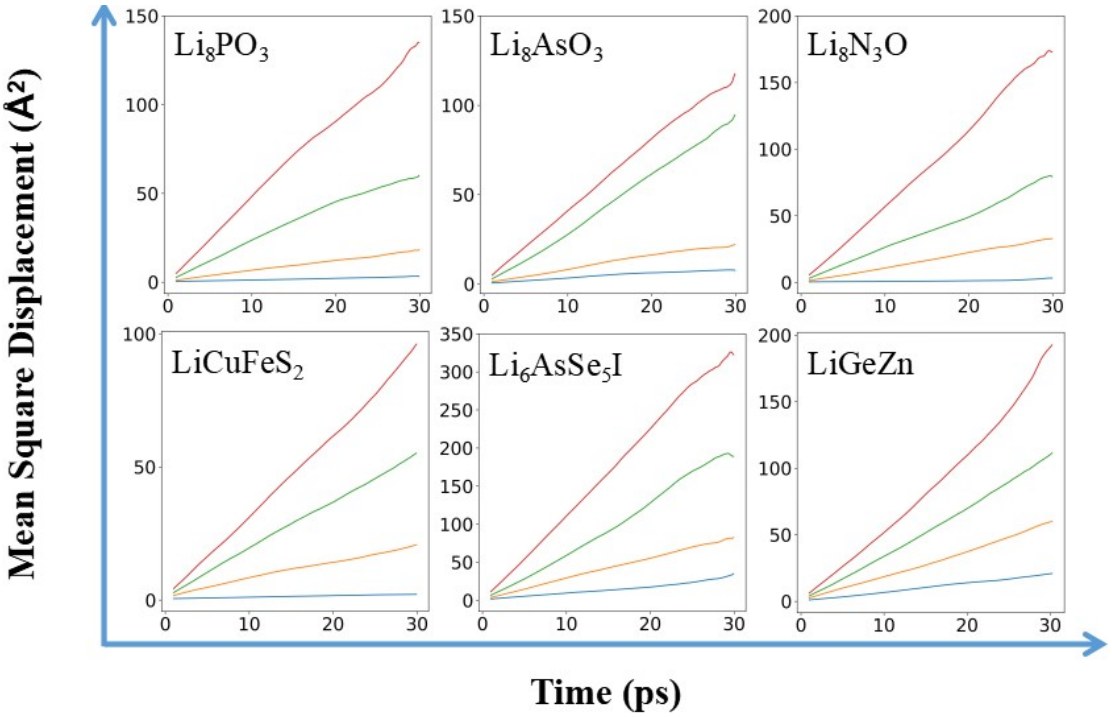

Figure S5. Lithium-ion Mean Squared Displacement (MSD) at different temperatures (red: 1500 K, green: 1200 K, yellow: 900 K, blue: 600 K).

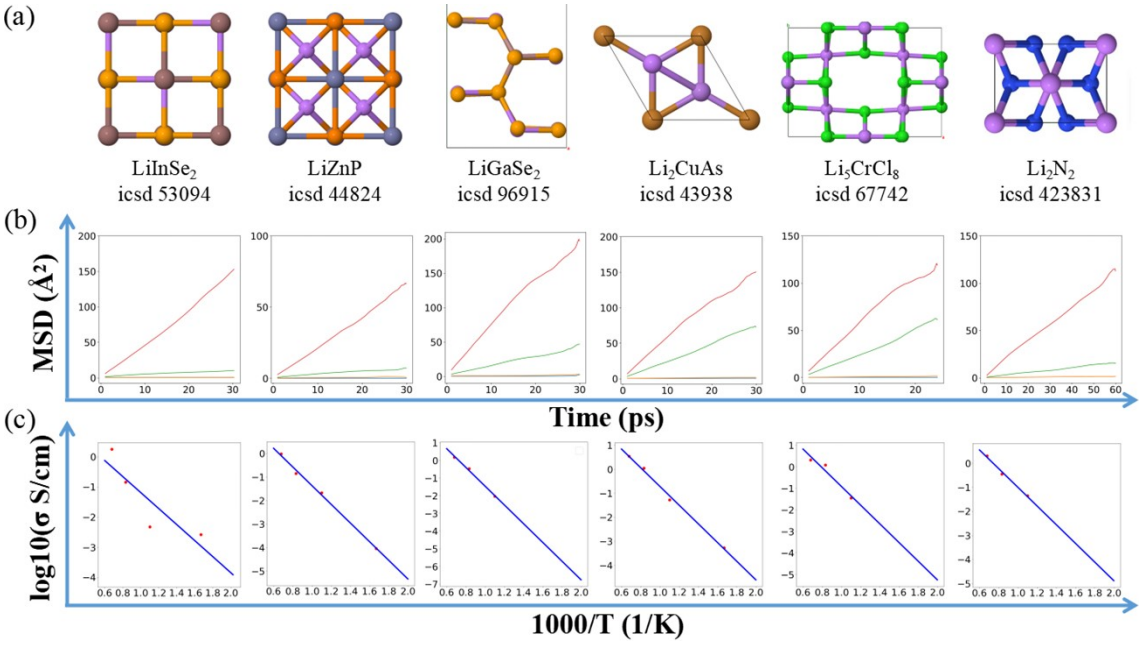

Figure S6. Evaluation of σ six compounds. (a) the crystal cell of six compounds; (b) Lithium-ion MSD at different temperatures, and (c) fitting graphs for the Arrhenius relationship between log(σ) and temperature (T).

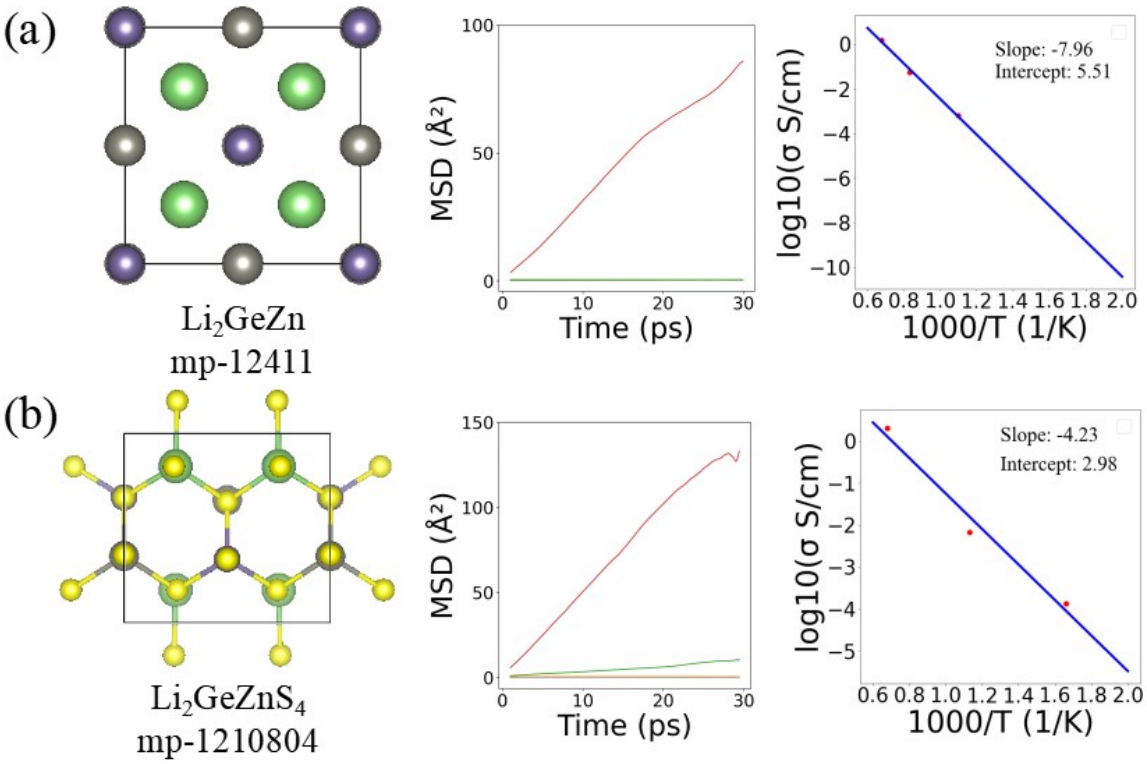

Figure S7. Evaluation of Li_2GeZn (a) and Li_2GeZnS_4 (b), including the crystal cell of compound, Lithium-ion MSD at different temperatures, and fitting graphs for the Arrhenius relationship between log(σ) and temperature (T).

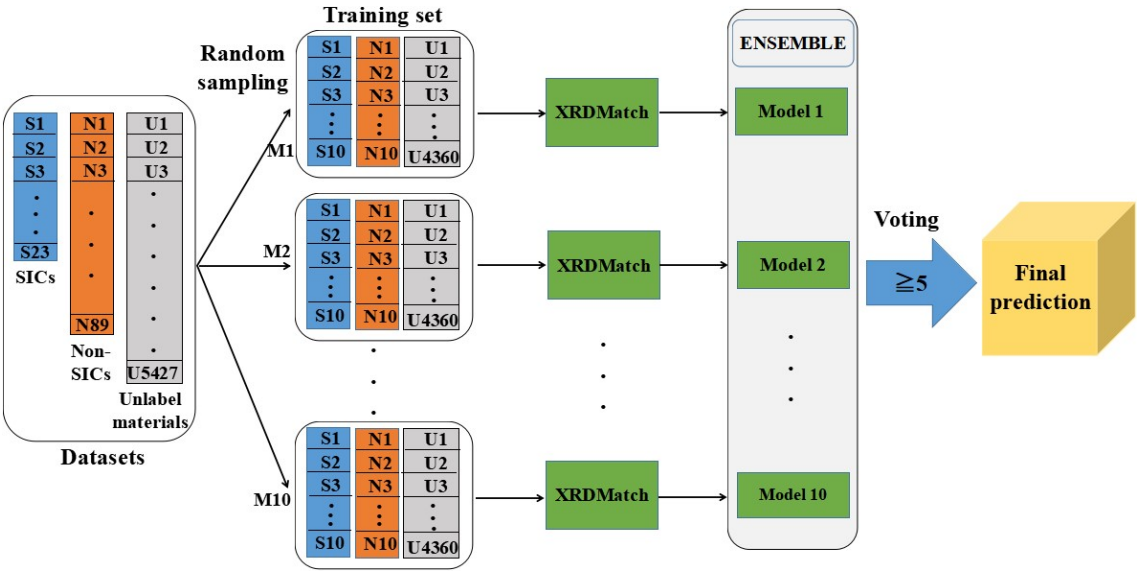

Figure S8. Schematic diagram of the ensemble model training process. We employ a random sampling approach to divide the labeled and unlabeled datasets into more diverse subsets as training set.

3. Experimental validation

3.1 Physicochemical characterization

The phase of the sample was characterized by powder X-ray diffraction. The XRD patterns were collected in the 2-theta range of 10°–80° using a diffractometer (D8 Advance, Bruker Corp.) at 36 kV, 20 mA. The sample was covered by an Kapton film during the measurement. The morphology of electrolyte was measured by scanning electron microscope (SEM, Nova NanoSEM 450, FEI company) equipped with energy dispersive spectroscopy (EDS).

3.2 Ionic and electronic conductivity test

The solid electrolyte powders were first pressed into pellets in model cells (ϕ = 10 mm) under 375 MPa using two stainless-steel rods as blocking electrodes. Ionic conductivity of the electrolyte was calculated by measuring the bulk resistance of the electrolyte pellet using potentiostatic electrochemical impedance spectroscopy (PEIS) on BioLogic VMP3 electrochemical workstation, in the frequency range of 7 MHz to 100 mHz with an amplitude of 10 mV. Electronic conductivity was determined by the DC polarization method at 0.3 V.

3.3 Cell assembly and electrochemical measurements

Composite cathode was prepared by ball mixing FeS_2 (Adamas, 99.99%), electrolyte and VGCF (mass ratio = 40:40:20) in a 30 mL zirconia pot at 200 rpm for 5 h. The mass ratio between the cathode and the zirconia ball was 1:10. 100 mg SE powder were cold-pressed at 375 MPa in a 10-mm diameter mold. Then, cathode powder was attached to the SEs at 250 MPa. Final, a Li/In alloy, consisting one piece of 50 μm Li foil (ϕ = 10 mm) and one piece 100 μm In foil (ϕ = 10 mm), was pressed onto the other side of SEs at 50 MPa. Copper foil and aluminum foil were employed respectively as the anode and cathode current collectors. The loading of FeS_2 is approximately 2 mg. Galvanostatic charge–discharge of cells at different current density (1C=894 mAh g^{-1}) was tested at voltage range from 1 to 3 V vs. Li/Li^+ (0.38 to 2.38 vs. Li-In/Li^+) on Neware CT4008Tn testing system. The cell was first cycled at 0.1 C and 0.2 C before the long cycle. All electrochemical measurements were tested at 30 °C with stack pressure of 50 MPa.

3.4 Table S3 ~ S2

Table S3. Room temperature ionic conductivity of LASeI samples under different sintering conditions.

Sintering conditions	without sintering	513 K	573 K	653 K	673 K
σ (S/cm)/ 25°C	2.6×10^{-5}	6.1×10^{-5}	9.1×10^{-5}	6.2×10^{-5}	3.2×10^{-5}

Table S4. Ionic conductivity at different temperatures calculated based on the total resistance, thickness, and area of cold pressed particles in the sample.

Temperature (K)	Contact area (cm^2)	Thickness (cm)	Total resistance (Ω)	Ionic conductivity (S/cm)	Log σ
293	0.785	0.05	875	7.28×10^{-5}	-4.1379
298	0.785	0.05	702	9.07×10^{-5}	-4.0422
303	0.785	0.05	580	1.12×10^{-4}	-3.9593
313	0.785	0.05	325	1.96×10^{-4}	-3.7078
323	0.785	0.05	212	3.00×10^{-4}	-3.5222

Table S5. The electronic conductivity at 25 ℃ of LASeI, calculated from the total resistance, thickness and area of the cold-pressed pellets.

Thickness (cm)	Diameter (cm)	Contact area (cm^2)	Current (A)	Voltage (V)	Resistance (Ω)	Electronic conductivity (S/cm)
0.05	1	0.785	1.50×10^{-7}	0.3	2.00×10^{6}	3.18×10^{-8}

3.5 Figure S9 ~ S11

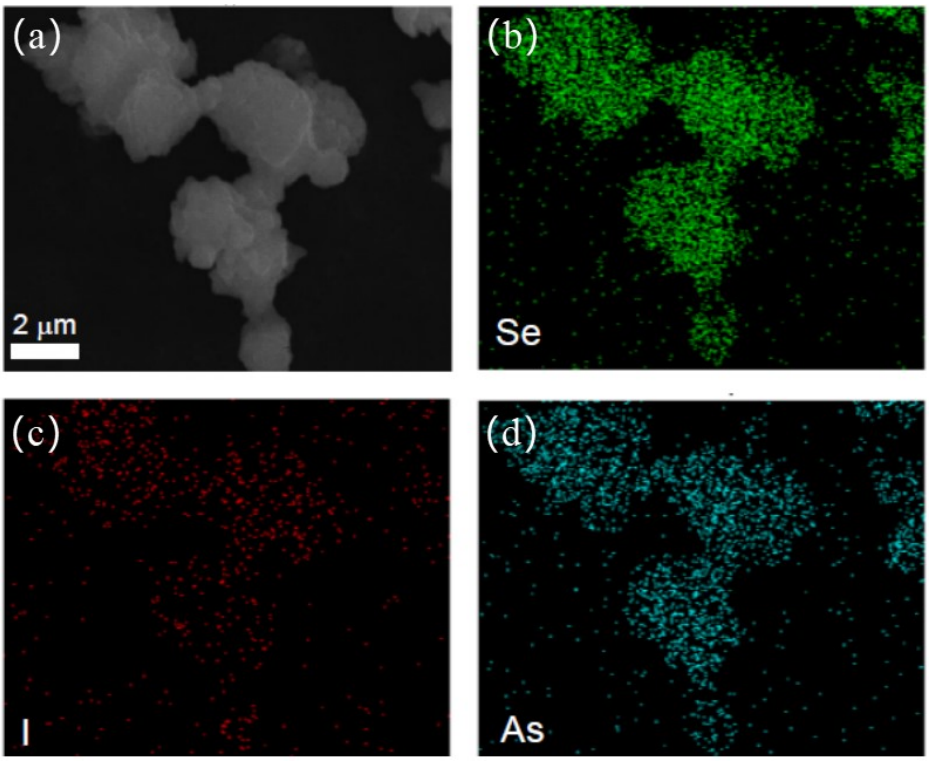

Figure S9. (a) TEM image the sample sintered at 573 K, (b-d) Selected-area element mapping analyses images of the sample.

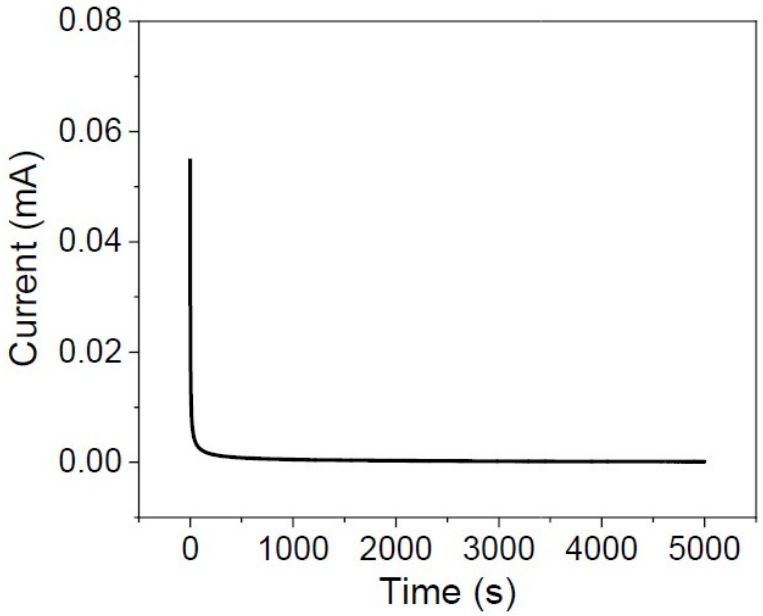

Figure S10. Direct current polarization of LASeI, which is tested in a cell configuration with stainless steel (SS) as blocking electrodeand solid electrolyte (SE) as separator at 25 ℃.

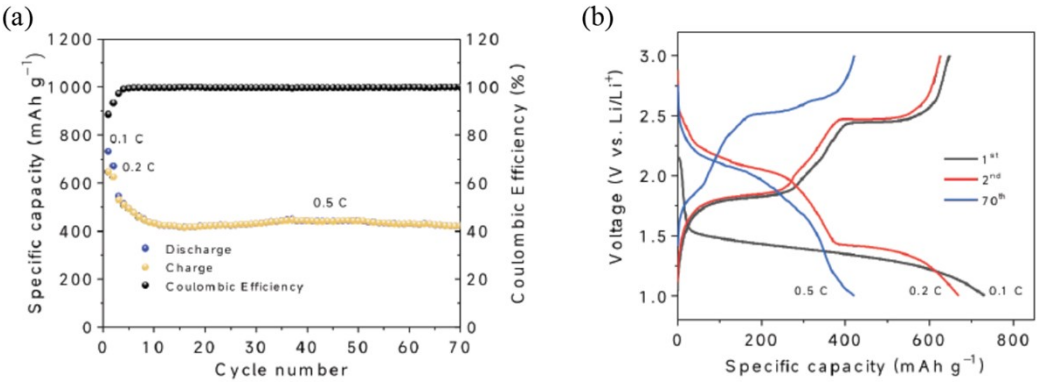

Figure S11. (a) The charge and discharge capacity and coulombic efficiency as a function of cycle number at different current densities for Li-In|LASeI|FeS_2 all-solid-state battery at 30 ℃. (b) The charge-discharge profiles of Li-In|LASeI|FeS_2 all-solid-state battery.

4. Diffusion mechanism

4.1 Figure S12 ~ S13

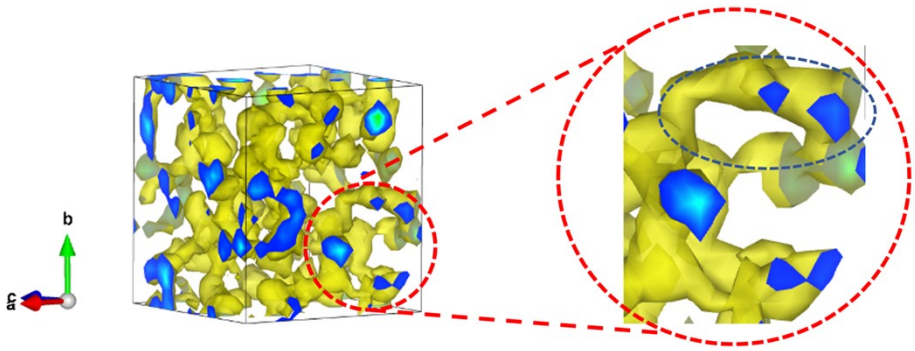

Figure S12. The Li-ion migration density plots of LASeI at 900 K, with the isosurface level set at 0.001/a0 (where a0 is the Bohr radius). The same migration cage is highlighted in both views within the red circle, while the blue circle marks the migration rings.

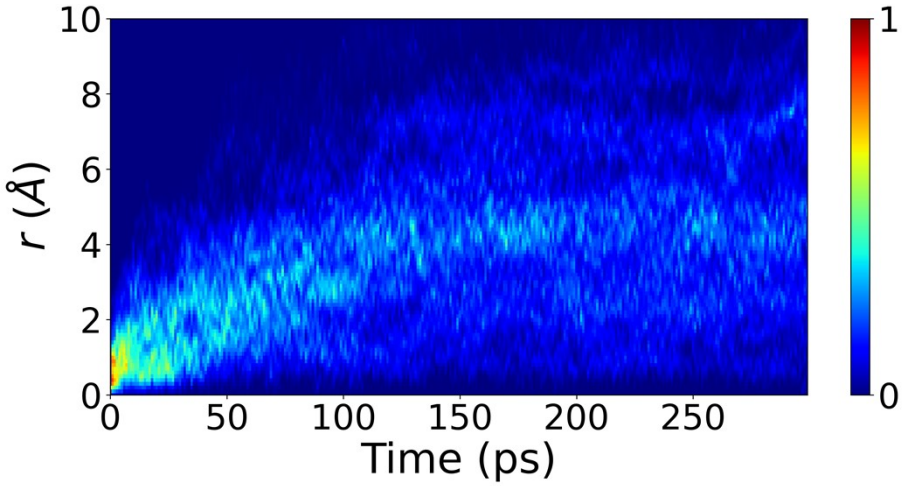

Figure S13. Van Hove correlation function for Li-Li in LASeI at 600 K.

5. Reference

[1] Lee, D.-H. et al. Pseudo-label: the simple and efficient semi-supervised learning method for deep neural networks. In ICML Workshop on Challenges in Representation Learning (2013).

[2] Rosenberg, C., Hebert, M., Schneiderman, H.: "Semi-supervised self-training of object detection models" (2005).

[3] Xie, Q., Luong, M.-T., Hovy, E., Le, Q.V.: "Self-training with noisy student improves ImageNet classification." In: Proceedings of the IEEE/CVF Conference on Computer Vision and Pattern Recognition, pp. 10687–10698 (2020).

[4] Sohn, K., Berthelot, D., Carlini, N., Zhang, Z., Zhang, H., Raffel, C.A., Cubuk, E.D., Kurakin, A., Li, C.-L.: "Fixmatch: Simplifying semi-supervised learning with consistency and confidence." Advances in neural information processing systems 33, 596–608 (2020).

[5] Bachman, P., Alsharif, O., Precup, D.: "Learning with pseudo-ensembles." Advances in neural information processing systems 27 (2014).

[6] Sajjadi, M., Javanmardi, M., Tasdizen, T.: "Regularization with stochastic transformations and perturbations for deep semi-supervised learning." Advances in neural information processing systems 29 (2016).

[7] Laine, S., Aila, T.: "Temporal ensembling for semi-supervised learning." arXiv preprint arXiv:1610.02242 (2016).

[8] Oviedo F, Ren Z, Sun S, Settens C, Liu Z, Hartono NT, Ramasamy S, DeCost BL, Tian SI, Romano G, Gilad Kusne A.: "Fast and interpretable classification of small X-ray diffraction datasets using data augmentation and deep neural networks." npj Computational Materials 5(1), 60 (2019).

[9] Wang, Hong, Yunchao Xie, Dawei Li, Heng Deng, Yunxin Zhao, Ming Xin, and Jian Lin.: "Rapid identification of X-ray diffraction patterns based on very limited data by interpretable convolutional neural networks." Journal of chemical information and modeling 60, 2004-2011 (2020).

[10] Grimme, S., Antony, J., Ehrlich, S., Krieg, H.: "A consistent and accurate ab initio parametrization of density functional dispersion correction (DFT-D) for the 94 elements H-Pu." The Journal of chemical physics 132(15) (2010).

[11] Kresse, G., Furthmüller, J.: "Efficient iterative schemes for ab initio total-energy calculations using a plane-wave basis set." Physical review B 54(16), 11169 (1996).

[12] Ong, S.P., Richards, W.D., Jain, A., Hautier, G., Kocher, M., Cholia, S., Gunter, D., Chevrier, V.L., Persson, K.A., Ceder, G.: "Python materials genomics (pymatgen): A robust, open-source python library for materials analysis." Computational Materials Science 68, 314–319 (2018).

[13] Cros, C., Hanebali, L., Latie, L., Gang, W., et al.: "Structure, ionic motion and conductivity in some solid-solutions of the LiClMCl2 systems (M= Mg, V, Mn)." Solid State Ionics 9, 139–147 (1983).

[14] Yamane, H., Kikkawa, S., Koizumi, M.: "Preparation and electrochemical properties of double-metal nitrides containing lithium." Journal of Power Sources 20(3-4), 311–315 (1987).

[15] Xia, W., Zhao, Y., Zhao, F., Adair, K., Zhao, R., Li, S., Zou, R., Zhao, Y., Sun, X.: "Antiperovskite electrolytes for solid-state batteries." Chemical Reviews 122(3), 3763–3819 (2022).Lapp, T., Skaarup, S., Hooper, A.: "Ionic conductivity of pure and doped Li3N." Solid State Ionics 11(2), 97–103 (1983).

[16] Lapp, T., Skaarup, S., Hooper, A.: "Ionic conductivity of pure and doped Li3N." Solid State Ionics 11(2), 97–103 (1983).

[17] Li, W., Wu, G., Xiong, Z., Feng, Y.P., Chen, P.: "Li+ ionic conductivities and diffusion mechanisms in Li-based imides and lithium amide." Physical Chemistry Chemical Physics 14(5),

1596–1606 (2012).

[18]Zhang, Y., He, X., Chen, Z., Bai, Q., Nolan, A.M., Roberts, C.A., Banerjee, D., Matsunaga, T., Mo, Y., Ling, C.: "Unsupervised discovery of solid-state lithium ion conductors." Nature Communications 10(1), 5260 (2019).

[19]Pereznieto, S., Jaafreh, R., Kim, J.-g., Hamad, K.: "Solid electrolytes for Li-ion batteries via machine learning." Materials Letters 337, 133926 (2023).

[20]Sendek, A.D., Cubuk, E.D., Antoniuk, E.R., Cheon, G., Cui, Y., Reed, E.J.: "Machine learning-assisted discovery of solid Li-ion conducting materials." Chemistry of Materials 31(2), 342–352 (2018).

[21]Landgraf, V., Famprikis, T., Leeuw, J., Bannenberg, L.J., Ganapathy, S., Wagemaker, M.: "Li5NCl2: A fully-reduced, highly-disordered nitride-halide electrolyte for solid-state batteries with lithium-metal anodes." ACS Applied Energy Materials 6(3), 1661–1672 (2023).

[22]Shi, X., Zeng, Z., Zhang, H., Huang, Y., Yan, C.-H., Du, Y.: "Encapsulating and operating a stable Li3ErBr6-based solid Li–SeS2 battery at room temperature." Advanced Functional Materials 33(15), 2213638 (2023).

[23]Chaomin, D., Cheng, M.: "Influence of aliovalent doping on the structure and property of Li2MnCl4 chloride solid electrolyte." Journal of University of Science and Technology of China 51(8), 628 (2021).

[24]Maletka, K., Ressouche, E., Rundloef, H., Tellgren, R., Delaplane, R., Szczepaniak, W., Zab-locka-Malicka, M.: "Phase transitions in the ionic conductor Li2UBr6 studied by neutron diffraction." Solid State Ionics 106(1-2), 55–69 (1998).

[25]Asai, T., Nishida, K., Kawai, S.: "Synthesis and ionic conductivity of Cu x Li3-xN." Materials Research Bulletin 19(10), 1377–1381 (1984).

[26]Lutz, H., Kuske, P., Wussow, K.: "Li2CrCl4 ein neuer Chloridspinell mit schneller Lithiumionenleitung." Naturwissenschaften 73, 623–623 (1986).

[27]Lopez, M., Veiga, M., Rodriguez-Carvajal, J., Fernandez, F., Jerez, A., Pico, C.: "The monoclinic perovskite La2LiSbO6. A Rietveld refinement of neutron powder diffraction data." Materials Research Bulletin 27(5), 647–654 (1992).

[28]Lutz, H., Zhang, Z., Pfitzner, A.: "Fast ionic conductivity of ternary iodides in the systems LiI-MIII2 (MII Mn, Cd, Pb)." Solid State Ionics 62(1-2), 1–3 (1993).

[29]Kanno, R., Takeda, Y., Yamamoto, O.: "Structure, ionic conductivity and phase transformation of double chloride spinels." Solid State Ionics 28, 1276–1281 (1988).

[30]Kanno, R., Takeda, Y., Yamamoto, O.: "Ionic conductivity of solid lithium ion conductors with the spinel structure: Li2MCl4 (M= Mg, Mn, Fe, Cd)." Materials Research Bulletin 16(8), 999–1005 (1981)

[31]Wickel, C., Zhang, Z., Lutz, H.: "Kristallstruktur und elektrische Leitfähigkeit von Li2–2xMn1+xCl4-Spinelltyp-Mischkristallen." Zeitschrift für anorganische und allgemeine Chemie 620(9), 1537–1542 (1994).

[32]Lutz, H., Partik, M., Schneider, M., Wickel, C.: "Ternary lithium halides, structure maps, characteristic M–X distances, and stability." Zeitschrift für Kristallographie-Crystalline Materials 212(6), 418–422 (1997).

[33]Ibarra, J., V´arez, A., Le´on, C., Santamarıa, J., Torres-Martınez, L., Sanz, J.: "Influence of composition on the structure and conductivity of the fast ionic conductors La2/3-xLi3xTiO3 ($0.03 \leq x \leq 0.167$)." Solid State Ionics 134(3-4), 219–228 (2000).

[34]Kanno, R., Takeda, Y., Takada, K., Yamamoto, O.: "Phase diagram and ionic conductivity of the lithium chloride-iron (II) chloride system." Solid State Ionics 9, 153–156 (1983).

[35]Ducros, J., Bach, S., Pereira-Ramos, J., Willmann, P.: "Optimization of cycling properties of the layered lithium cobalt nitride Li2.20Co0.40N as negative electrode material for Li-ion batteries." Electrochimica Acta 167, 20–24 (2015).

[36]Badot, J., Panabiere, E., Emery, N., Dubrunfaut, O., Bach, S., Pereira-Ramos, J.: "Percolation behaviors of ionic and electronic transfers in Li3-2xCo xN." Physical Chemistry Chemical Physics 21(5), 2790–2803 (2019).

[37]Jimenez, R., Rivera, A., Varez, A., Sanz, J.: "Li mobility in Li0.5-xNaxLa0.5TiO3 perovskites ($0 \leq x \leq 0.5$): Influence of structural and compositional parameters." Solid State Ionics 180(26-27), 1362–1371 (2009).

[38]Percival, J., Apperley, D., Slater, P.: "Synthesis and structural characterisation of the Li-ion conducting garnet-related systems, Li6AlLa2Nb2O12 (A= Ca, Sr)." Solid State Ionics 179(27-32), 1693–1696 (2008).

[39]Awaka, J., Kijima, N., Takahashi, Y., Hayakawa, H., Akimoto, J.: "Synthesis and crystallographic studies of garnet-related lithium-ion conductors Li6CaLa2Ta2O12 and Li6BaLa2Ta2O12." Solid State Ionics 180(6-8), 602–606 (2009).

[40]Galven, C., Fourquet, J.-L., Crosnier-Lopez, M.-P., Le Berre, F.: "Instability of the lithium garnet Li7La3Sn2O12: Li+/H+ exchange and structural study." Chemistry of Materials 23(7), 1892–1900 (2011).

[41]Log´eat, A., K¨ohler, T., Eisele, U., Stiaszny, B., Harzer, A., Tovar, M., Senyshyn, A., Ehrenberg, H., Kozinsky, B.: "From order to disorder: The structure of lithium-conducting garnets Li7-xLa3TaXZr2-xO12 (X= 0–2)." Solid State Ionics 206, 33–38 (2012).

[42]Kamaya, N., Homma, K., Yamakawa, Y., Hirayama, M., Kanno, R., Yonemura, M., Kamiyama, T., Kato, Y., Hama, S., Kawamoto, K., et al.: "A lithium superionic conductor." Nature Materials 10(9), 682–686 (2011).

[43]Matsuda, Y., Sakamoto, K., Matsui, M., Yamamoto, O., Takeda, Y., Imanishi, N.: "Phase formation of a garnet-type lithium-ion conductor Li7-3xAlxLa3Zr2O12." Solid State Ionics 277, 23–29 (2015).

[44]Bron, P., Johansson, S., Zick, K., Gunne, J., Dehnen, S., Roling, B.: "Li10SnP2S12: An affordable lithium superionic conductor." Journal of the American Chemical Society 135(42), 15694–15697 (2013).

[45]Kaib, T., Bron, P., Haddadpour, S., Mayrhofer, L., Pastewka, L., Jarvi, T.T., Moseler, M., Roling, B., Dehnen, S.: "Lithium chalcogenidotetrelates: Licht synthesis and characterization of new Li+/Sn/Se compounds." Chemistry of Materials 25(15), 2961–2969 (2013).

[46]Kwon, O., Hirayama, M., Suzuki, K., Kato, Y., Saito, T., Yonemura, M., Kamiyama, T., Kanno, R.: "Synthesis, structure, and conduction mechanism of the lithium superionic conductor Li10+δGe1+δP2-δS12." Journal of Materials Chemistry A 3(1), 438–446 (2015).

[47]Mukhopadhyay, S., Thompson, T., Sakamoto, J., Huq, A., Wolfenstine, J., Allen, J.L., Bernstein, N., Stewart, D.A., Johannes, M.: "Structure and stoichiometry in supervalent doped Li7La3Zr2O12." Chemistry of Materials 27(10), 3658–3665 (2015).

[48]Paik, B., Oguchi, H., Sato, T., Takagi, S., Dorai, A., Kuwata, N., Kawamura, J., Orimo, S.-i.: "Ionic conduction in Li3Na(NH2)4: Study of the material design for the enhancement of ion conductivity in double-cation complex hydrides." AIP Advances 9(5) (2019).

[49]Kanno, R., Takeda, Y., Takahashi, A., Yamamoto, O., Suyama, R., Kume, S.: "New double chloride in the LiCl CoCl2 system: II. Preparation, crystal structure, phase transformation, and ionic conductivity of Li2CoCl4 spinel." Journal of Solid State Chemistry 71(1), 196–204 (1987).

[50]Baral, A.K., Narayanan, S., Ramezanipour, F., Thangadurai, V.: "Evaluation of fundamental transport properties of Li-excess garnet-type Li5+2xLa3Ta2-xYxO12 (x= 0.25, 0.5 and 0.75) electrolytes using AC impedance and dielectric spectroscopy." Physical Chemistry Chemical Physics 16(23), 11356–11365 (2014).

[51]Chen, Y., Rangasamy, E., Liang, C., An, K.: "Origin of high Li+ conduction in doped Li7La3Zr2O12 garnets." Chemistry of Materials 27(16), 5491–5494 (2015).

[52]Phraewphiphat, T., Iqbal, M., Suzuki, K., Matsuda, Y., Yonemura, M., Hirayama, M., Kanno, R.: "Syntheses, structures, and ionic conductivities of perovskite-structured lithium–strontium–aluminum/gallium–tantalum-oxides." Journal of Solid State Chemistry 225, 431–437 (2015).

[53]Deiseroth, H.-J., Kong, S.-T., Eckert, H., Vannahme, J., Reiner, C., Zaiß, T., Schlosser, M.: "Li6PS5X: A class of crystalline Li-rich solids with an unusually high Li+ mobility." Angewandte Chemie International Edition 47(4), 755–758 (2008).